SANDIA REPORT

SAND2021-11442
Printed September 2021

Sandia National Laboratories

DNS/LES Study of Representative Wall-Bounded Turbulent Flows using SIERRA/Fuego

Heeseok Koo, John C. Hewson, Alexander L. Brown, Robert C. Knaus, Andrew Kurzawski, Michael D. Clemenson

Prepared by
Sandia National Laboratories
Albuquerque, New Mexico 87185
Livermore, California 94550

Issued by Sandia National Laboratories, operated for the United States Department of Energy by National Technology & Engineering Solutions of Sandia, LLC.

Available to DOE and DOE contractors from

U.S. Department of Energy
Office of Scientific and Technical Information
P.O. Box 62
Oak Ridge, TN 37831

Telephone: (865) 576-8401
Facsimile: (865) 576-5728
E-Mail: reports@osti.gov
Online ordering: http://www.osti.gov/scitech

Available to the public from

U.S. Department of Commerce
National Technical Information Service
5301 Shawnee Road
Alexandria, VA 22312

Telephone: (800) 553-6847
Facsimile: (703) 605-6900
E-Mail: orders@ntis.gov
Online order: https://classic.ntis.gov/help/order-methods

ABSTRACT

This report summarizes a series of SIERRA/Fuego validation efforts of turbulent flow models on canonical wall-bounded configurations. In particular, direct numerical simulations (DNS) and large eddy simulations (LES) turbulence models are tested on a periodic channel, a periodic pipe, and an open jet for which results are compared to the velocity profiles obtained theoretically or experimentally. Velocity inlet conditions for channel and pipe flows are developed for application to practical simulations. To show this capability, LES is performed over complex terrain in the form of two natural hills and the results are compared with other flow solvers. The practical purpose of the report is to document the creation of inflow boundary conditions of fully developed turbulent flows for other LES calculations where the role of inflow turbulence is critical.

ACKNOWLEDGMENT

The authors would like to thank the SIERRA/Fuego development team for assistance during the development of this work. The authors would also like to thank Kathryn Gabet Hoffmeister and Lindsay Gilkey for providing thoughtful reviews of this report.

CONTENTS

LIST OF FIGURES

LIST OF TABLES

NOMENCLATURE

DNS Direct Numerical Simulation

LES Large Eddy Simulation

RANS Reynolds Averaged Navier-Stokes

CVFEM Control-Volume Finite-Element

CFD Computational Fluid Dynamics

Re Reynolds number

Re_τ Friction-based Reynolds number

h Channel height

k Turbulent kinetic energy

S Strain rate tensor

u Velocity

u^+ Dimensionless velocity

u_τ Shear velocity

y^+ Wall coordinate

Δ Filter size

μ Molecular viscosity

μ_{eff} Effective viscosity

μ_t Turbulent eddy viscosity

ν Kinematic viscosity

ρ Density

τ_w Wall shear stress

1. INTRODUCTION

As computing capabilities increase, so do the capabilities to simulate increasingly complex flows. As with many computational physics models, fluid mechanics simulations are dependent in large part on accurate definition of the boundary conditions. Historical average flow models using steady-state approximations and Reynolds Averaged Navier-Stokes (RANS) equations only require mean flow input for simulation predictions. More resolved techniques like Large Eddy Simulation (LES) require complex input to represent the complexity of the surface behavior at selected boundary locations. How the boundary conditions are specified impacts the quality of the subsequent predictions. Under-resolved fluid mechanics techniques often employ boundary layer approximations to simulate the shear effect of a wall boundary layer. This is because fully resolving the dynamics of a boundary layer for every application is not always possible. This work explores some of these issues and works to develop, implement, and validate capabilities in SIERRA/Fuego [20].

Atmospheric flows are a component of fire, flow, and dispersion simulations, and their implementation SIERRA/Fuego should be characterized. We seek to further the credibility of the modeling and simulation work through exploration of model accuracy. This takes the form of model verification and validation. Verification assesses the accuracy of the numerical solution of the computational model (e.g. by comparing to analytical solutions). Validation assesses the accuracy of the simulation by direct comparison to experimental data. One of many guidelines for validation techniques can be found in [18]. Prior validation work in this area can be found in Brown and Benavidez [5]. Here, we are concerned with rural and urban contaminant dispersion predictions. A recent review summarizes much of the historical work in this area [15].

Rather than being specifically concerned with plume transport, this effort is more generally concerned with the boundary layer and boundary conditions, as well as validation to selected problems of relevant interest. Turbulent jets are another boundary condition that can benefit from this level of characterization, and they can be found in a range of application spaces such as fires, materials processing, and turbine blade cooling.

This work seeks to develop and validate turbulent inflow boundary conditions in SIERRA/Fuego. SIERRA is an architecture of various solvers for simulating engineering physics problems that is developed and maintained by Sandia National Laboratories (SNL), and Fuego is the low-Mach fluid mechanics solver that targets reacting flows. Fuego has the ability to be coupled with other SIERRA applications such as models for radiation, heat transfer, and solid mechanics.

Fuego offers an extensive number of RANS turbulent flow models. However, to meet an increasing demand to better represent turbulence-chemistry interactions, LES capabilities were recently implemented in Fuego. LES directly solves for large-scale motions while scales smaller than the filter size, usually the mesh size, are modeled. By simulating development of unsteady

eddies in the flow, LES has shown superior predictive capabilities of chemical reactions compared to RANS based models [23]. Therefore, it is important to understand the capability of the LES models present in Fuego to guarantee reliability of the solver and accuracy of the results.

We perform model verification on canonical flow configurations (specifically channel and pipe flow) in a effort to reveal requirements for mesh resolution and model selection by comparing to theoretical predictions. The results of these simulations are translated to inflow boundary conditions and applied to geometry that represents a real system for comparison with experimental data. We chose experimental configurations of terrain scenarios where predictions from other CFD codes are available to compare to Fuego results.

1.1. Turbulent Flow Models

Before discussing the numerics relevant to this study, we will highlight the unique features of the Fuego discretization scheme. While a number of fluid dynamic solvers are discretized in finite volume or conservative finite difference, Fuego is written in a control-volume finite-element (CVFEM) formulation to achieve higher-order spatial accuracy while keeping the conservative property of finite volume codes. Therefore, Fuego may require different mesh resolution or numerics from the reference DNS/LES studies which typically use finite volume or spectral methods. Fuego contains many common features with other low-Mach turbulent flow solvers such as central-differencing and SIMPLE-based continuity correction. Other features of the solver include the use of an unstructured mesh, node-based degrees of freedom, and pressure-velocity collocation at nodes.

Two LES models are available in Fuego: the Smagorinsky model and subgrid-kinetic-energy (k^{sgs}) one-equation model. The LES filtered Navier-Stokes equations are closed with a model for the sub-grid turbulent eddy viscosity (μ_t). In the Smagorinsky model, this closure takes the form of

$$\mu_t = \rho (C_s \Delta)^2 |\tilde{S}| \tag{1.1}$$

where ρ is the density, C_s is a model constant, Δ is the filter size, and $\tilde{S}$ is the magnitude of the Favre-filtered strain rate tensor.

The subgrid turbulent eddy viscosity in the one equation closure is defined by

$$\mu_t = C_{\mu_\varepsilon} \Delta k^{sgs\frac{1}{2}} \tag{1.2}$$

where C_{μ_ε} is a model constant. The subgrid kinetic energy, k^{sgs}, is computed using the following transport equation

$$\frac{\partial \bar{\rho} k^{sgs}}{\partial t} + \frac{\partial \bar{\rho} \tilde{u_j} k^{sgs}}{\partial x_j} = \frac{\partial}{\partial x_j} \left(\frac{\mu_t}{\sigma_k} \frac{\partial k^{sgs}}{\partial x_j} \right) + P_k^{sgs} - D_k^{sgs} \tag{1.3}$$

where u_j is the velocity, σ_k is a model constant, the production (P_k^{sgs}) and dissipation (D_k^{sgs}) terms are modeled, and the Favre-filter is represented by $\tilde{\cdot}$ and the spatial filter is represented by $\bar{\cdot}$.

An appropriate boundary condition is required for the subgrid kinetic energy transport equation. We note that the k as it appears in RANS-based models (e.g. $k-\varepsilon$ and $k-\omega$) is used to model the time-averaged energy of the velocity components and differs from k^{sgs}, which models kinetic energy due to fluctuations that occur at length scales smaller than the spatial discretization.

For both the Smagorinsky and one-equation models, the coefficients C_s and C_{μ_ε} can be either predetermined or dynamically computed. Dynamic models rely on local gradients that are typically underpredicted in unstructured solvers. Therefore, turbulent viscosity is typically smaller than when the predetermined coefficient is used.

Spatial accuracy is limited to second-order so that a linear sub-element profile can be assumed. Unlike a staggered grid system, the pressure-velocity collocated solver is prone to numerical instability. In this study, the tested mesh resolutions and time-step size allow the use of central differencing for the momentum equations. Upwinding is used for the subgrid kinetic energy. For the terrain simulations, additional upwinding is added to account for a large spatial discretization.

LES models require a wall model to sustain an appropriate velocity gradient normal to the wall [19]. Several wall models are available in Fuego, but only one is suitable for LES. The k^{sgs} model at the wall is fixed at

$$k^{sgs} = \frac{u_\tau^2}{C_\mu^{1/2}} \tag{1.4}$$

which we note is a RANS model that may require correction, and an iterative approach is used to compute wall shear stress (τ_w). The iterative approach is also used for the Smagorinsky model as it does not solve for k^{sgs}. Other model details are available in Fuego user manual [20].

2. ANALYSIS OF WALL-BOUNDED FLOW SIMULATIONS FOR USE AS INFLOW BOUNDARY CONDITIONS

Given the unique features of the CVFEM formulation used in Fuego, it is important to understand the behavior of conventional wall models and their grid resolution requirements for a range of Reynolds numbers. As dense grids can increase accuracy at the expense of computational cost, we begin with direct numerical simulation (DNS) of channel and pipe flows at lower Reynolds numbers. We explore both the standard structured mesh and a layered mesh that retains resolution at the wall and improves the aspect ratio near the center plane. DNS becomes prohibitively expensive for the target Reynolds number of the terrain simulations where the channel inflow boundary condition will be applied. Therefore, we examine the output of the LES model forms on the same channel geometry with special attention given to the modeling of the shear stress at the wall. Results from each simulation are compared to the theoretical viscous and log-law layer velocity profiles given in wall units.

2.1. Channel Flow DNS

Channel flow is one of the simplest turbulent flow simulations due to the absence of a mean wall normal velocity component, a statistically stationary state, and orthogonality of the geometry. Parameterization of the baseline DNS simulation follow Moser et al. [17]. We note that the domain size is known to alter turbulent flow structures due to periodic boundary conditions and lengthy turbulent flow streaks. The domain size should be large enough such that the periodic assumption is not damaged by any large-scale vortex structures. The baseline domain (Fig. 2-1) has dimensions of 2π x 2 x π with periodic boundaries in the x and z directions and walls on the y boundaries. A second mesh where the dimensions were doubled in the x and z directions was created to verify the adequacy of the baseline mesh.

The friction-based Reynolds number, Re_τ, is defined by the wall shear velocity $u_\tau = \sqrt{\tau_w/\rho}$ and half channel height h, where τ_w is the wall shear stress and ρ is the fluid density.

$$Re_\tau = \frac{u_\tau h}{\nu} \tag{2.1}$$

In an incompressible flow, Re_τ is the wall unit of the half channel height. For instance, $y^+ = 395^+$ at the half channel height for a flow of Re_τ=395, where y^+ is given by

$$y^+ = \frac{u_\tau y}{\nu} \tag{2.2}$$

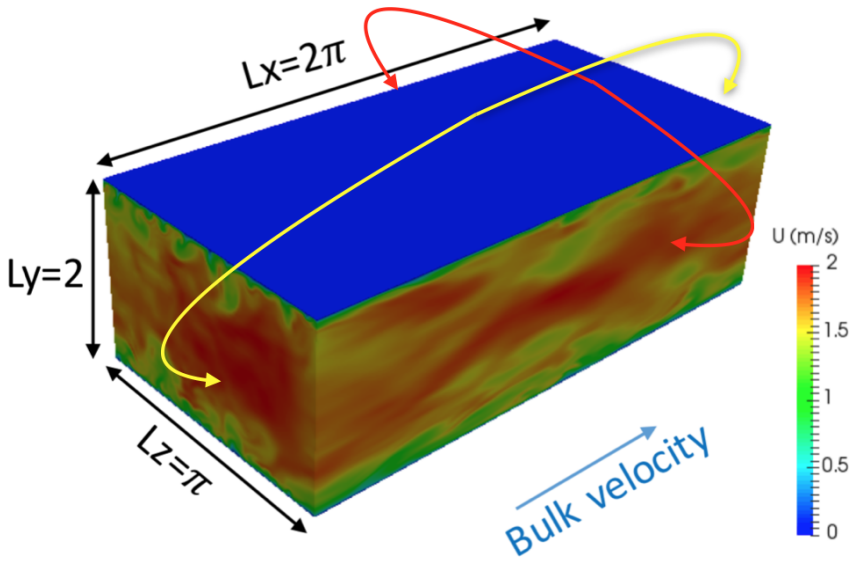

Figure 2-1. Channel configuration for DNS with example stream-wise velocity contours. Arrows indicate connected periodic boundaries in the stream-wise (yellow arrow) and span-wise (red arrow) direction.

This simplifies the definition of the mesh resolution for the given turbulence level and channel dimension as y^+ is known.

A set of computations was performed with a mesh of fully structured hexahedron elements. Several mesh resolutions were tested as listed in Table 2-1. Mesh discretizations are normalized by the wall unit (denoted with superscript $^+$) for a flow of Re_τ=395. For the baseline mesh, the resolution in the wall-normal direction increases from y^+ of 1.04 at the wall to 40 at the center plane while the dicretization in the stream-wise and span-wise directions are constant. The table also lists maximum cell aspect ratio, which decreases as the mesh is refined. Figure 2-2 (left) shows an example of the maximum aspect ratio occurring at the wall.

Table 2-1. DNS channel mesh resolutions. Re_τ=395 for all simulations and 'Extended' refers to the meshes with the doubled domain. [1]Baseline mesh. [2]Maximum aspect ratio occurs at the center plane.

Name	$\Delta x \times (\Delta y_{min}\text{-}\Delta y_{max}) \times \Delta z$	Mesh Size	Re_{bulk}	Max Aspect Ratio
Base	26 × (1.04-40) × 19.5	0.4M	21,500	25[1]
Base Extended	26 × (1.04-40) × 19.5	1.7M	17,400	25
M2	13 × (0.68-40) × 10	2.0M	16,700	19.1
M2 Extended	13 × (0.68-40) × 10	7.9M	16,200	19.1
M3	8.7 × (0.68-40) × 6.4	4.5M	15,700	12.8
M4 a	6.5 × (1.08-40) × 4.9	7.1M	15,400	8.2[2]
M4 b	6.5 × (0.68-40) × 4.9	7.9M	15,500	9.6
Layered	6.5-26 × (1.04-40) × 4.9-19	4.0M	12,300	6.2

The second DNS case used layered meshes to keep the maximum aspect ratio at approximately 6 (Fig. 2-2 right). Two layers of wedge-shape meshes were added to increase the stream-wise and

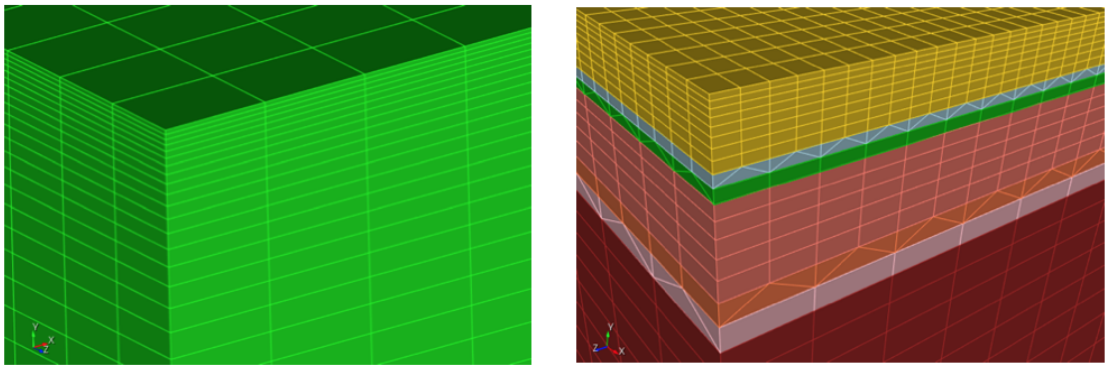

Figure 2-2. DNS meshes zoomed in near a corner. Structured hexahedron mesh with growth away from the wall (left) and layered mesh with two wedge transition layers (right).

span-wise element size at the center plane to four times (two times per layer) that of the size at the wall. The maximum discretization corresponds to the 0.4 million element baseline mesh, while the near-wall resolution of the layered mesh matches the finest non-layered meshes (Tab. 2-1).

Flow was initialized by superimposing a parabolic laminar velocity profile with sinusoidal waves and random fluctuations as shown in Figure 2-3. The flow becomes fully turbulent after approximately one second of simulated time, after which flow data is collected for application as an inflow boundary. This fully developed flow was used as an initial condition to save computational cost when simulating different mesh resolutions and running LES models.

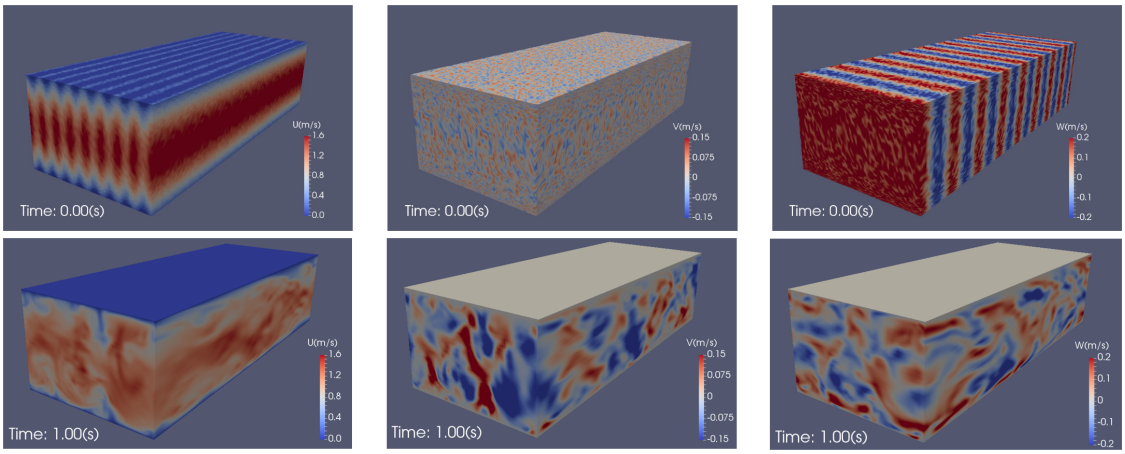

Figure 2-3. Example from LES of initialization method at time zero (top row) and at 1 second (bottom row). From left to right is stream-wise, wall-normal, and span-wise velocity contours. Simulation data is collected from 1 second onward for the inflow file.

A body force was imposed to prevent the flow from slowing down due to the wall friction. The forcing value is specified in a Fuego simulation as $F = \tau_w A$ where A is the wall area (both upper and lower walls) and τ_w is obtained from the target Re_τ. While τ_w fluctuates due to turbulence, the forcing preserves the bulk velocity and Re_τ. The flow is assumed to have reached a statistically stationary state once the bulk velocity begins to fluctuate around the target value.

The mean stream-wise velocity profile is obtained by averaging in both time and the periodic directions once a statistically stationary state was reached. Velocity profiles for the meshes listed in Table 2-1 are shown in Figure 2-4. The viscous layer profile is captured well in each mesh. In all of the structured mesh cases, 'energetic' velocity profiles are observed in which the velocities (u^+) are larger than the theoretical log layer profile.

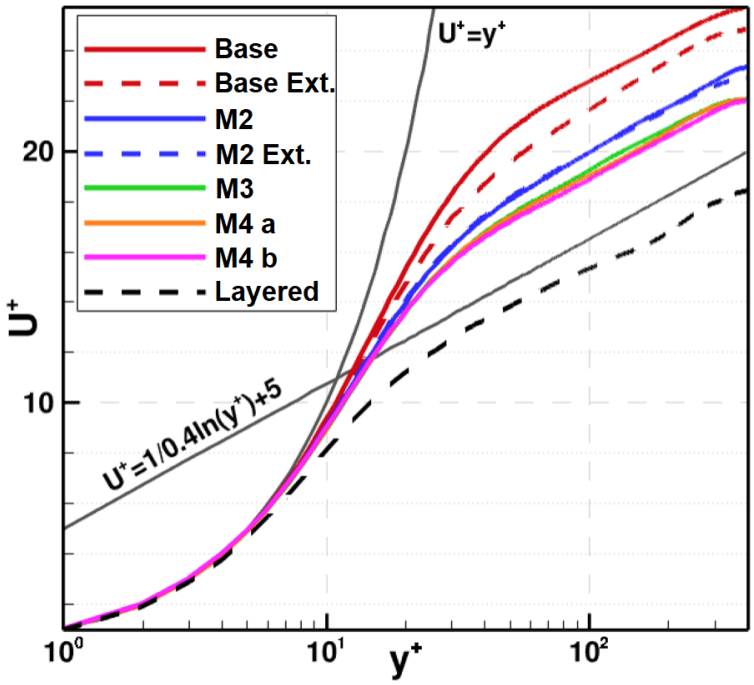

Figure 2-4. DNS velocity profiles from the structured meshes and the layered mesh listed in Table 2-1 for $Re_\tau = 395$.

Grid refinement of the structured meshes was made on the stream-wise and span-wise directions with the base mesh being the coarsest and M4 being the finest. It can be seen that using a finer mesh improves the velocity profile in the log region, but there is little difference between M3 and M4. Additionally, the extended domain only improved the base mesh, but not the next finest mesh (M2). All of the structured mesh simulations over-predicted the velocity in the log-law region, overshooting the target bulk Reynolds number of 12000 by at least 3000.

The layered mesh with wedge element transitions provides a method for keeping the cell aspect ratio below 6.2 everywhere in the domain. The layered mesh result in Fig. 2-4 shows that the velocity profile is now under-predicted in the log-law region. Kravchenko et al. note that adding more mesh layers helps to alleviate under-prediction in the log layer [14].

2.2. Pipe Flow DNS

Pipe flow DNS was performed on a cylindrical mesh with a length of four diameters. Figure 2-5 shows the computational domain with streamwise velocity contours as well as the non-layered and layerd meshes. The domain is periodic in streamwise direction as marked in the figure. Near

the wall, the wall normal mesh size decreases with a fixed rate similar to the channel cases. Similar to the channel case, the layered mesh shown in Figure 2-5 was generated to alleviate extremely stretched cells near the wall. Due to the lengthening in the azimuthal direction near the wall, the maximum cell aspect ratio was set to 10 which is nearly twice that of the channel. The layered mesh consists of approximately 400 thousand elements and two wedge transition layers.

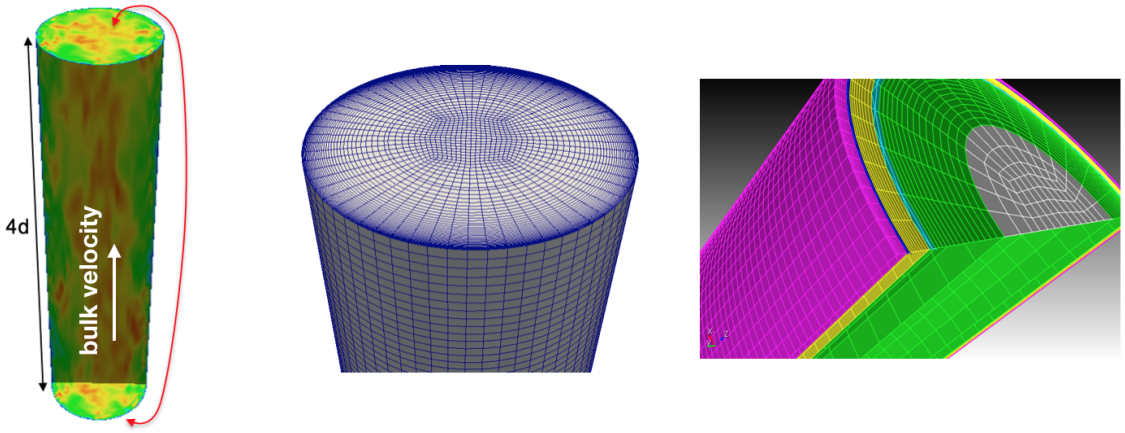

Figure 2-5. Pipe domain with velocity contours (left) and two mesh systems: hexahedron (center) and layered (right).

The averaged velocity profiles using two non-layered meshes and one layered mesh are plotted in Fig. 2-6. Overall, similar trends to the channel simulations were observed. Both the coarser (400 thousand elements) and dense (1.8 million elements) simulations over-predict the mean velocity in the log-layer, while the layered mesh simulations reduced over-prediction of the average velocity in the log-layer. At layers where cell size abruptly changes, the mean velocity profile is visibly less smooth than the non-layered profiles, i.e. at y^+=40.

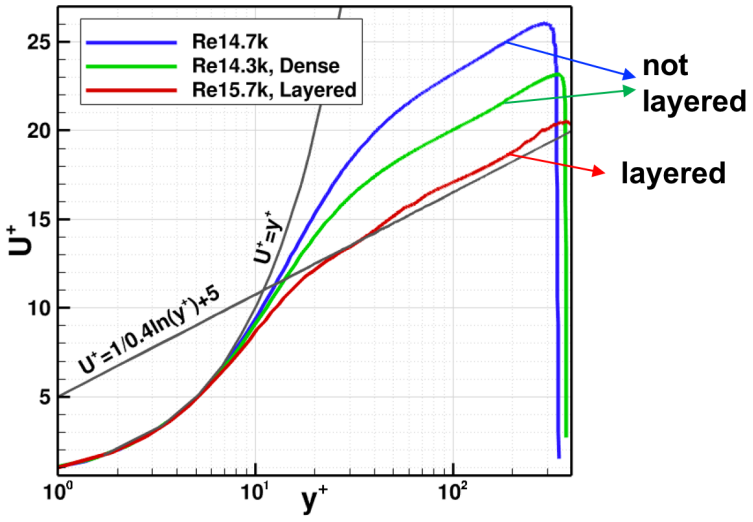

Figure 2-6. Mean velocity profiles for different DNS mesh resolution/shapes for similar bulk Reynolds numbers.

2.3. Channel Flow LES

Using DNS at the higher Reynolds numbers required for inflow data generation can be prohibitively computationally expensive. LES offers a less expensive alternative, but care must be taken in the formulation of the wall boundary. In this section, we investigate the effect of the location of the first off-wall velocity using a range of Reynolds numbers, three mesh resolutions, and two LES turbulence closure formulations.

2.3.1. Wall Treatment

Fuego version 4.48 supports two wall boundary conditions: 'laminar' and 'turbulent' [20]. A 'laminar' wall is applied for laminar and turbulent flow models which do not involve unresolved kinetic energy (k). This boundary condition uses strong Dirichlet enforcement where a no-slip condition is directly applied on the wall nodes. Viscous flux between the first two nodes (see Fig. 2-7) is computed using the effective viscosity (μ_{eff}), which is the sum of the molecular viscosity (μ) and turbulent viscosity (μ_t).

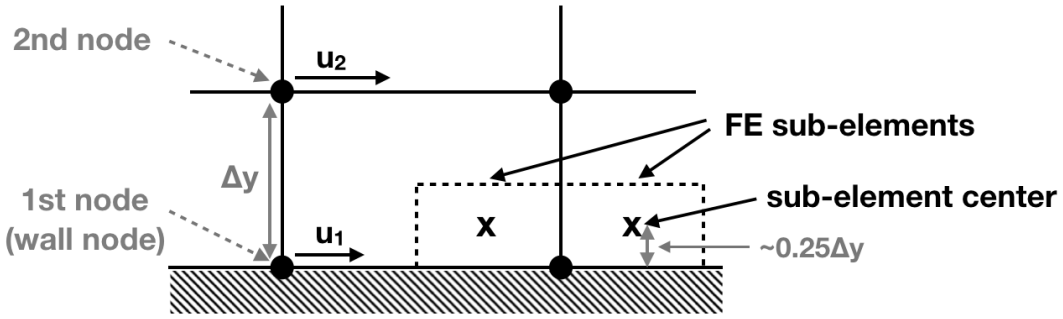

Figure 2-7. Near wall elements and nodes.

A 'turbulent' wall condition is applied for turbulent flow models that are based on computing k. The wall node is allowed to have non-zero velocity such that the shear stress between the first two nodes uses μ_{eff} and the velocity difference $u_2 - u_1$. At the wall, viscous flux or the wall shear (τ_w) exists which is modeled by various wall models. Fuego either models wall shear using k or directly uses the first off-wall velocity. The wall shear is found through a Newton iteration by assuming the velocity obeys a log-law or viscous layer profile based on the location of the first off-wall node in wall units. This approach does allow for the use of non-kinetic energy based turbulence models.

Numerical challenges arise when applying boundary conditions in a vertex node based solver. Traditionally, boundary node values are enforced following Economon et al. [8], which is similar to the no-slip 'laminar' condition described above. However, this approach indirectly forces part of the wall elements to have a wall property which may induce numerical wall roughness at sharp edges (e.g. corner nodes). A quick remedy is (as described in Poinsot [10]) to have the first layer of cells parallel to the boundary surface.

Alternatively, a slip condition can be applied on the boundary. The physical meaning of the first node velocity (u_1 in Fig. 2-7) is extensively discussed in Poinsot [10]. The paper shows that the slip condition results in superior accuracy compared to the no-slip strong-Dirichlet condition. Also described in Poinsot is the limitation of the slip approach near a corner. For a vertex-based system, a node will be located on the corner and the direction of the velocity applied by the slip condition is not clear. Poinsot ultimately recommends the use of applying a wall model to the first off-wall node and a no-slip condition to the wall node to alleviate the corner issue.

Fuego uses a CVFEM formulation in which sub-element components are temporarily defined for higher-order flux calculations. On a hexahedron mesh, the center of the first sub-element lies at approximately 1/4 the height of the first element marked as 'x' in Figures 2-7 and 2-8. Sub-element velocities are reconstructed from nodal velocities using a finite element basis functions. The basis function at the first node is uniform such that velocity at the sub-element center is equivalent to the velocity at the adjacent wall node, allowing the sub-element center location to be used for the wall model calculations. This follows a similar concept to Fig. 7(a) of [10] with $\delta \sim \frac{1}{4}\Delta y$. Then, the wall function can be applied on the sub-element center using the wall node velocity u_1. An alternative approach that is more widely used in the finite volume community is to apply the wall model at the second node location and directly use u_2 and Δy (see Fig. 2-8).

While there are a number of wall models available in literature, Fuego calculates the wall shear using a wall function method in models where the turbulent kinetic energy is transported. In this method, wall shear is computed based on the assumption that velocity profile follows a log-law for $y^+ > 11.68$ and a viscous layer profile below that point. The turbulent kinetic energy can be directly incorporated into the model or a Newton iteration can be used with a velocity at a given location. Figure 2-8 compares the aforementioned two locations where the model could be applied. This location selection matters for both the Newton iteration and k-based wall shear calculations.

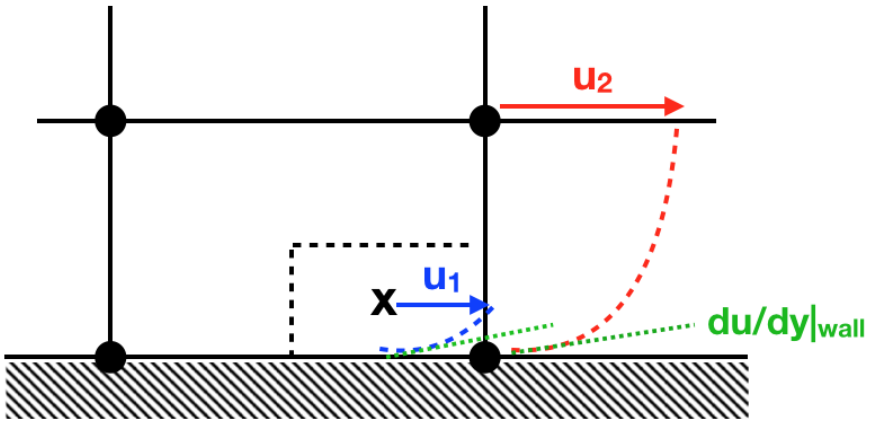

Figure 2-8. First off-wall velocity at either the second node (red) or the center of the sub-element (blue). The velocity gradient at the wall is marked in green.

Note that the wall model alters the velocity at the first off-wall location that is either the center of the sub-element or the 2nd node. Some wall models modify μ_t on a number of near-wall

elements, however this has not been attempted in Fuego. Ultimately, a key driver for retaining a substantial velocity gradient between the wall and the first off-wall location is the lack of μ_t in the wall shear calculation [10].

In RANS-based turbulent flow models, the turbulent kinetic energy is

$$k_{RANS} = \frac{1}{2}\widetilde{u_k'' u_k''} \tag{2.3}$$

while in LES, k is given by

$$k_{LES} = \frac{1}{2}(\widetilde{u_k u_k} - \tilde{u}_k \tilde{u}_k) \tag{2.4}$$

where the $\tilde{\cdot}$ represents a Favre filter and $\cdot''$ is the fluctuating component of the velocity. The definitions are different in that k_{LES} is the spatially unresolved energy of a filtered volume at any given time whereas k_{RANS} includes k_{LES} and the energy from an unsteady fluctuating motion that is captured by LES. Therefore, k_{RANS} is normally much larger than k_{LES}, although this difference diminishes near the wall where unsteady turbulent fluctuations are small. A careful differentiation between RANS and LES is needed for k boundary conditions and wall model implementations. In RANS, k is set such that $u_\tau = C_\mu^{1/4} k^{1/2}$ and $k_{wall} = u_\tau^2 / C_\mu^{1/2}$, while a k_{wall} value of zero is better suited for LES.

2.3.2. Numerical Assessment

We seek to compare the options of prescribing turbulent wall boundary conditions in LES by running simulations at a range of Reynolds numbers listed in Table 2-2. Simulations with both the Smagorinsky and one-equation (k^{sgs}) turbulence models were performed on the LES case with a Reynolds number of 6,000 to compare the choice of the location of the wall-modeled velocity (see Fig. 2-9 left). The two LES closure models predict nearly identical velocity profiles and all subsequent results will be of the k^{sgs} model. Among the k^{sgs} simulations, when using the sub-element center, there was little difference between calculating the wall sheer from a Newton iteration or the RANS relation ($u_\tau = C_\mu^{1/4} k^{1/2}$). When the wall model is applied to the second node, the velocity profile shifts up and begins on the theoretical log-law line. Likewise, when the 'laminar' no-slip boundary condition is applied to the Smagorinsky model, the velocity at the first sub-element center shifts down to zero.

Figure 2-9 (right) compares three LES cases as well as DNS using the baseline mesh where the second node velocity is used to calculate the wall shear stress. The second node velocity (i.e. the beginning of the line shown in the plot) aligns well with the theoretical velocity profiles. Non-dimensionalized mesh size increases significantly as Reynolds number goes up due to the dependence on the shear velocity (see Tab. 2-2). We note that regardless of the Reynolds number, an S-shape, or a flow acceleration away from the wall is observed. It is presumed that the lack of μ_t blending is the reason for the DNS-like S-shape. For instance, if μ_t decreases near the wall, the

t

Table 2-2. DNS baseline and LES flow conditions and mesh resolutions expressed in wall units.

Simulation Name	Re_τ	$\Delta x \times \Delta y_{min} \times \Delta z$ (in wall unit$^+$; on the baseline mesh)
DNS	395	$26 \times 1.04 \times 19$
LES	1,500	$98 \times 3.9 \times 71$
LES	6,000	$390 \times 15.6 \times 285$
LES	60,000	$3{,}900 \times 156 \times 2{,}850$

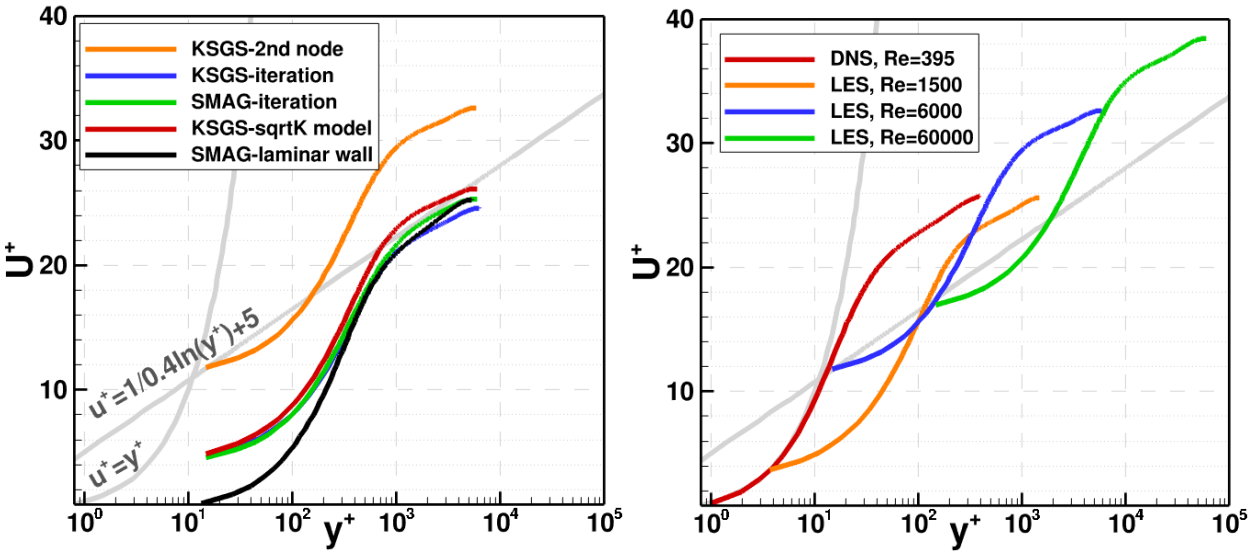

Figure 2-9. Velocity plots of different model choices using the LES with $Re_\tau =$ 6,000 (left). Velocity plots of four Reynolds numbers presented in Table 2-2 using the second node to calculate wall shear stress (right).

shear force could be balanced without the acceleration. This trend alters velocity profiles far from the wall and should be thoroughly investigated in future work.

In addition to the baseline mesh from Table 2-1, two coarser meshes were created by varying the mesh size in only the wall normal direction to investigate the effect of cell skewness and poor near-wall mesh resolution on wall model simulations results. The maximum aspect ratios are 25, 5, and 1.3 for the baseline, coarse 1, and coarse 2 meshes respectively (see Tab. 2-3).

Table 2-3. Baseline and two coarser meshes.

	nx × ny × nz	Δy_{min} / half channel width	Maximum element aspect ratio
Baseline	$96 \times 72 \times 64$	1/380	25
Coarse 1	$96 \times 64 \times 64$	1/75	5
Coarse 2	$96 \times 40 \times 64$	1/20	1.3

Figure 2-10 focuses on the LES case where the Reynolds number is 6000 with the baseline and two coarser meshes. The first off-wall node velocity using the second node approach aligns well

with the theoretical velocity profile (the log-law or viscous layer, colored in gray). For the sub-element center approach, the first node velocity, marked in 'x', matches to the theoretical profile at the sub-element center location. Using the baseline mesh, the sub-element center location is in the viscous layer while the second node is in the log-law layer. Additionally, as the element aspect ratio improves, the S-shape trend becomes less severe.

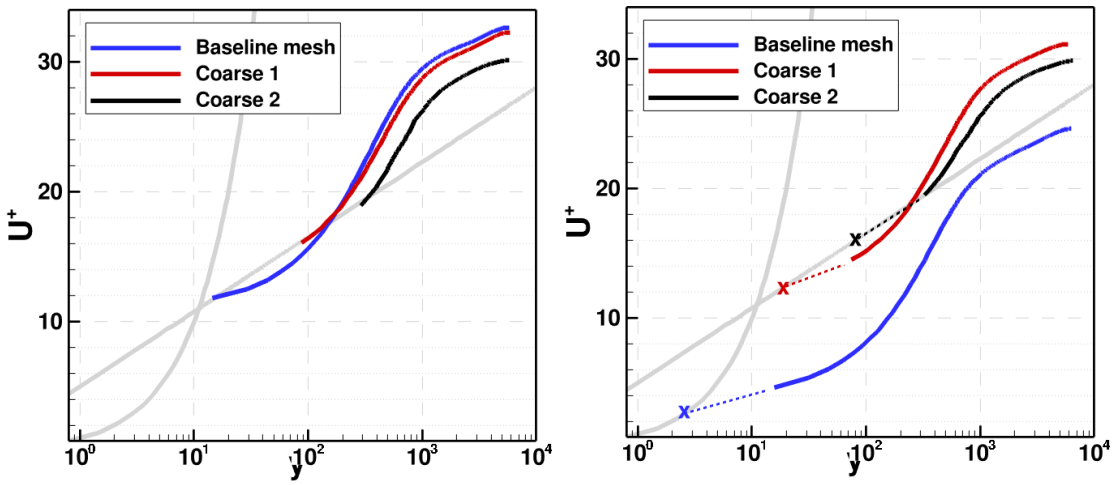

Figure 2-10. Different mesh resolution results for Re_τ equals 6,000 using the second node (left) and the center of sub-element (right) as the first off-wall velocity. On the right plot, the wall node velocity is marked with an X on the sub-element center locations and extended by dash lines to the second.

The two approaches show very different results, which becomes more apparent when plotted on a linear scale (Fig. 2-11). On coarser meshes, both sub-element center and second node locations are in the log-law region, and the velocity profiles are clustered around higher values than the log-law profile. The near wall velocity is similar between all cases except the sub-element center baseline mesh case, which is closer to the log-law profile away from the wall.

The same trend is observed in the other two Reynolds number cases (see Fig. 2-12), where predictions are improved in the log-law region if both sub-element center and second node locations are in the viscous region. However, the 'S'-curve shape remains even if the first off-wall location is in the log-law region. These observations indicate that as long as the first sub-element center is in the viscous sublayer ($y^+ < 11.6$), the model tends to match the log-law layer profile far from the wall. Keating and Piomelli [12] diagnosed that the 'S'-curve appears due to the lack of wall normal fluctuations and the inflection point is related to the mesh size in two wall-parallel directions (x and z). Therefore, unless we can afford more resolution in x and z directions, random forcing may be needed to reduce the strength of the 'S'-curve.

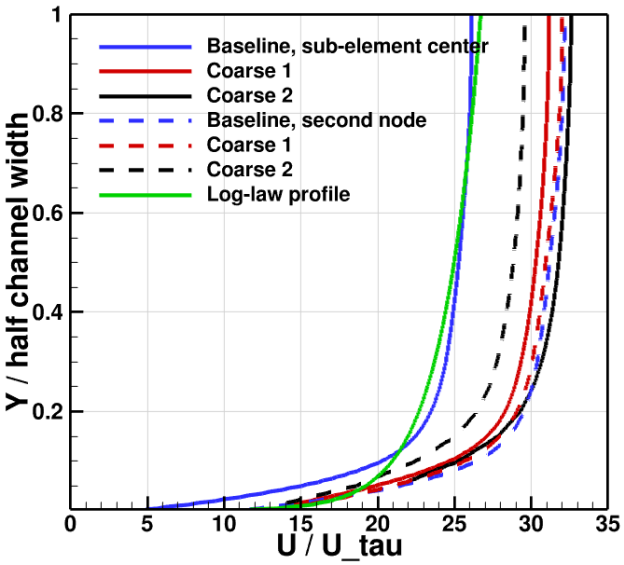

Figure 2-11. Linear scale velocity plots of various wall approaches. Solid lines and dashed lines are sub-element center and second node approaches, respectively. The green line is the log-law profile.

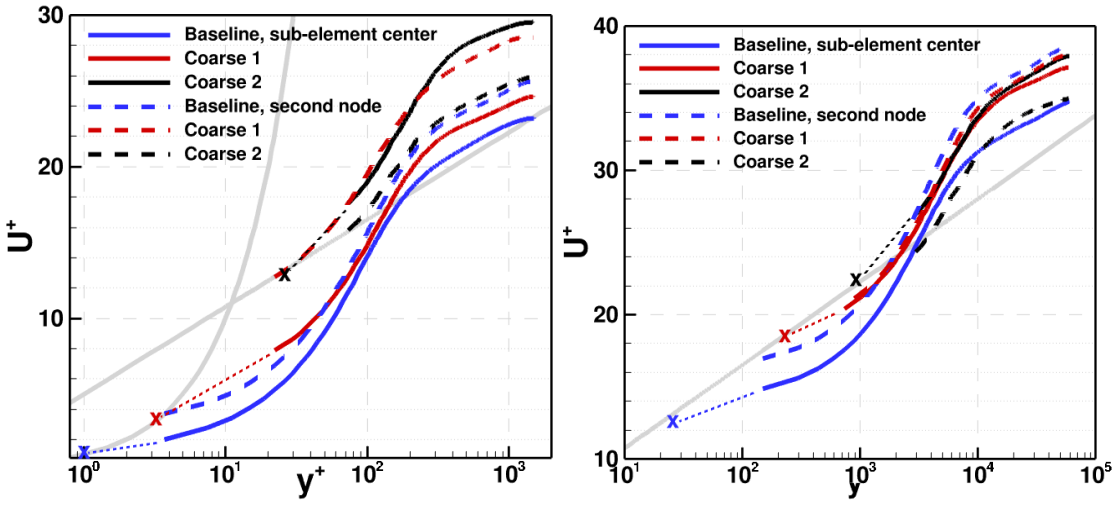

Figure 2-12. Wall approaches of different meshes are compared for Re_τ of 1,500 (left) and 60,000 (right) flows. Solid lines and dashed lines are the sub-element center and second node approaches, respectively.

2.4. General Discussion

The simulation activity detailed in this section represents among the first efforts to characterize the turbulent wall behavior of SIERRA/Fuego in the near-wall region for LES flow conditions. This work is differentiated from other similar work in the LES literature in that SIERRA/Fuego uses the CVFEM formulation. With RANS based and lower resolution LES simulations, the wall functions are normally used to prescribe the wall interactions with the domain. This effort removed the wall functions, and focused the mesh such that the log and linear regimes of u^+/y^+ behavior were resolved using a variety of turbulence model assumptions. The results show that with adequate resolution, the code will produce a flow that approaches the expected theoretical behavior.

The channel flow simulations provide the basis for developing a turbulent inflow boundary for a variety of cases (Section 2.1). By extracting surface predictions, a solution consistent flow may be extracted and scaled to a different flow and domain. The channel flow simulations are employed to produce such a flow condition in support of work on a variety of applications (e.g. inflow boundary conditions for natural terrain, flow through an urban landscape). By solution consistency, we imply that the joint solution to the momentum and continuity equations are satisfied for the boundary condition. These inflow conditions are also temporally respective of the way turbulent flows evolve at inflow interfaces. These features are not recoverable from random number generator based turbulent inlet specifications that can represent the statistical mean and variability of a turbulent flow, but not the coherence. Inflows lacking in coherence will be more dissipative than is physical and less realistic for simulating flow conditions. Hence these inflow assumptions are superior, being able to prescribe a coherent flow consistent with the solver system in the code.

The pipe/channel flow work shows boundary layer behavior similar to the baseline simulation work with the rectangular domain (Section 2.2). An approximate reproduction of the wall boundary layer is found in the results. Mesh resolution is similarly important.

In the numerical assessment sub-section 2.3.2, the Reynolds number is increased to explore the accuracy of the predictions beyond DNS conditions. The principle finding here is that away from the wall the predictions are reasonably approximate; however, the near-wall predictions are not necessarily accurate depending on the location of the node or sub-element center velocity used in the wall model.

This work focuses on the viscous boundary layer for a scenario lacking thermal advection. Were thermal gradients are present, the results might differ. The resolution of advective behavior may be more dependent on the off-normal mesh resolution due to the buoyant condition at the interface. The work herein may show some adequacy for isothermal scenarios; however, it may be necessary to explore non-isothermal conditions with higher resolution to allow the buoyant behavior to develop through the viscous wall layers of the flow. Improving (lowering) the cell aspect ratio near the wall for convection scenarios may be necessary when extending this work to problems with a thermal component.

3. GENERATION AND USE OF A FULLY-DEVELOPED TURBULENT INFLOW FILE

Unlike RANS-based turbulence models, it can take time for turbulence to develop when using LES or DNS. For example, in a pipe flow starting from a bulk flow, laminar or RANS models reach a fully developed velocity profile at approximately 1 diameter length downstream. DNS requires 50-200 diameters of stream-wise length to reach a stationary state. The length depends on the initial condition, mesh resolution, numerics, and critically, Reynolds number. Weaker turbulence requires a longer distance to become fully turbulent, and poor mesh resolution and/or diffusive numerics may fail to sustain or even trigger turbulent fluctuations.

In LES it would require an enormous computational resource for a non-turbulent inflow to reach a turbulent state before it interacts with a target geometry. Even if sufficient turbulent structures are seen, obtaining a correct velocity profile presents another challenge. Therefore, using fully developed turbulence from an auxiliary simulation at an inflow boundary has become popular in LES. The auxiliary simulation is carefully controlled to guarantee a correct turbulent profile.

Figure 3-1 illustrates the application of an inflow boundary from an auxiliary simulation to the target scenario. The auxiliary simulation runs until turbulence in the channel or pipe becomes fully developed. At selected planes in the channel or pipe, the velocity components are stored in a file referred to as the 'inflow file' for a sufficient time span. The stored velocity data are directly used in a target simulation that has an inflow boundary similar to a pipe or channel in shape. This process may need to be rescaled to adjust the bulk velocity, physical dimensions, and time scale. If this is the case, the user must select the appropriate velocity and length rescaling based on the problem and use these to calculate the appropriate time scale (i.e. time scale equals length scale divided by velocity scale).

Difficulties associated with this inflow file approach include an artificial periodicity introduced when the simulation time reaches the end of the collected inflow data. Additionally, maintaining a statistically stationary channel or pipe flow is challenging for a compressible flow due to the conversion of pressure forcing into thermal energy. That is, the Mach number slowly decreases and temperature increases within the collection time frame, making rescaling of the flow field difficult. To overcome these issues, several turbulent inflow models were proposed that produce inflow turbulence without an auxiliary simulation [16, 13, 11]. However, it is widely believed that those models are not universally applicable since the model parameters rely heavily on the numerical implementation of the CFD code. On the other hand, the inflow file approach is much less sensitive to solver details. as the velocities produced by this approach can be applied to a different piece of software that supports user-specified inflow conditions.

The inflow file procedure was tested in Fuego on three scenarios: two terrain features using the channel flow and one pipe flow case. For the terrain simulations, the lower half of the channel was

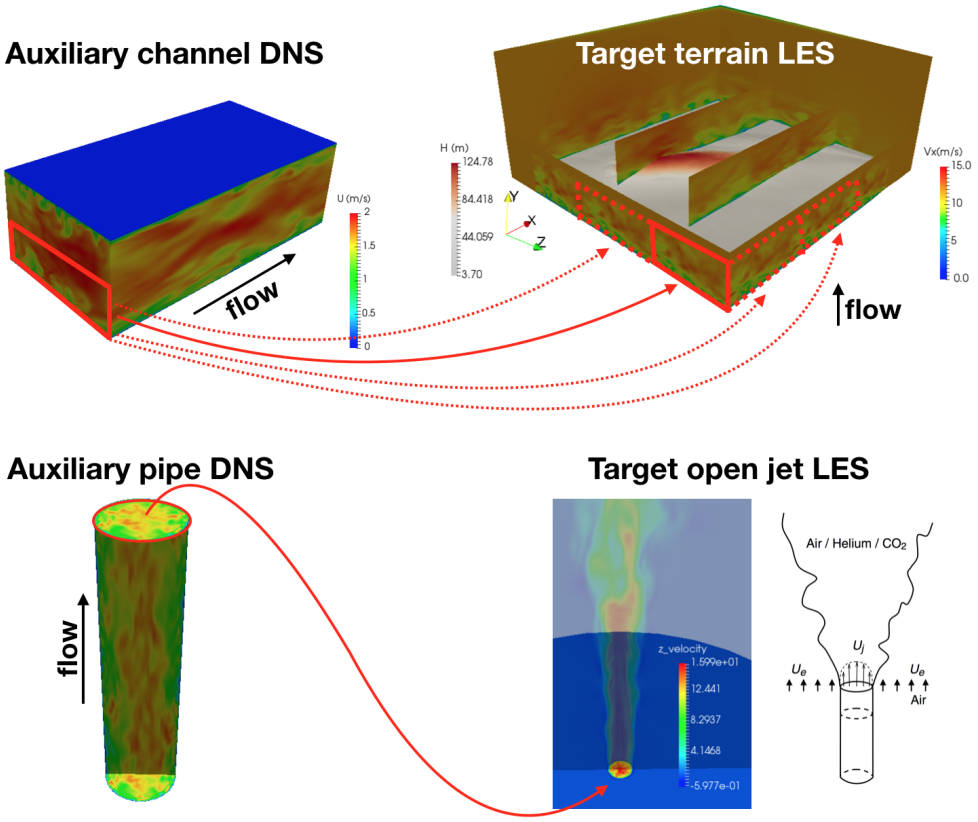

Figure 3-1. Examples of the inflow file approach. Top: A terrain LES example that uses half of a channel DNS/LES profile, where the same file is copied to multiple dashed inflow planes. Bottom: An open jet LES example using a pipe DNS/LES inflow.

used as an incoming fully-developed atmospheric boundary layer (See Fig. 3-1, top). A channel LES with a sufficiently large Reynolds number (60,000) was modified to match the measured velocity profile near the ground. Pipe DNS inflow datasets are used for an open jet LES. Several inflow datasets were prepared to adapt to the turbulence intensity variation of a target flow with bulk Reynolds numbers of 7,000, 18,000, 23,400, 32,000, and 58,300 (Fig. 3-1, bottom).

3.1. Terrain Simulation Using Channel LES

Prediction of a flow over complex terrain extends the application space of SIERRA/Fuego beyond the targeted small-to-medium scale fire applications. Two terrain examples are shown here: Askervein hill [21] and Bolund hill [3]. Askervein hill (Fig. 3-2) is in Scotland, UK which is one of the simpler but larger terrain hills that are frequently modeled using CFD. The height of the hill is 116 m and the domain spans 2 km wide. Bolund hill (Fig. 3-3) is a 12 m high hill located in Denmark and has a steep face opposing the wind which makes prediction of the velocity profile more difficult than the smoother Askervein hill. For both cases, the wind passes over flat ground before reaching the hill. Bolund hill is surrounded by water for many kilometers while upstream

of Askervein hill is a few kilometers of flat vegetation approaching the Atlantic ocean. Bolund hill was used as a reference case where many researchers submitted and compared results against experimental measurements at a workshop [4]. For the comparison, modelers were given an inflow velocity profile. For Askervein hill, no such systematic comparisons have been performed.

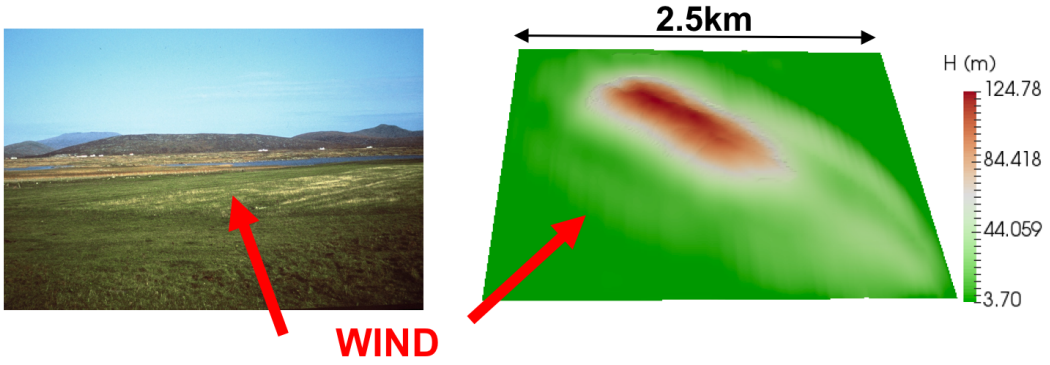

Figure 3-2. Askervein hill (left) and the LES domain (right) [22]. Wind direction is indicated by red arrows.

Figure 3-3. Bolund hill (left) and the LES domain (right) [2]. Wind direction is indicated by red arrows.

The lower half of a channel simulation with a shear Reynolds number of 60,000 was used as a fully developed boundary layer inflow for the hill simulations. Rescaling was performed such that the velocity profile matched the observed velocity profile at the upstream location. The Bolund hill includes the upstream velocity profile which was used to rescale the inflow file. Since the atmospheric boundary layer does not necessarily have the same boundary layer thickness definition, matching near-ground velocity is an acceptable alternative approach. Figure 3-4 compares the measured velocity profile and the rescaled profile using Re_τ=60,000 inflow data. Note that there was an error in the rescaling process of the Bolund hill inflow leading to a substantial discrepancy in the profile as well in the simulation result. For the Askervein hill, a boundary layer with five times the thickness was used given that the incoming stream went through vegetation for several kilometers before reaching the hill. Velocity components were adjusted to match the south-western direction of the inflow for both cases.

The meshes were generated from terrain files using Cubit. The height of the domain is selected such that top boundary condition does not affect the flow near the ground. Mesh size and

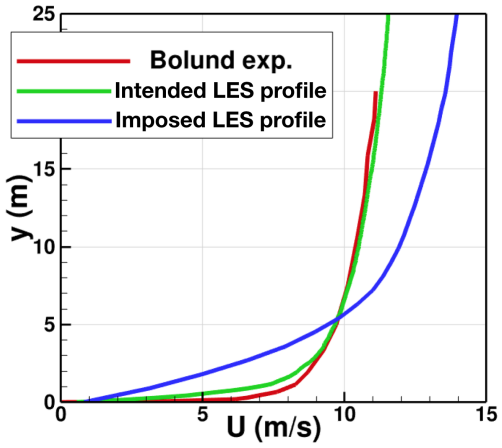

Figure 3-4. Inflow velocity profile provided to Bolund hill modelers and imposed in LES.

resolution information is listed in Table 3-1. The Bolund hill scenario in particular was challenging to mesh due to the sharp angle of the cliff on the leading edge of the domain (Fig. 3-5). The meshes were highly skewed in this region, since conformal hexahedral meshes were used for the domain. While this was not a significant component of the exhibit of the results, it was a complicating topic in the lead-up to the simulation production work.

Table 3-1. Mesh information used for the terrain simulations.

	Domain size	Δx, Δz	Δy_{min}	Total meshes
Askervein hill	2.5×2.5×1km	25m, 25m	2.5m	0.65M
		15m, 15m	1.5m	2.6M
		10m, 10m	1m	8.8M
Bolund hill	0.2×0.2×0.1km	1m, 1m	0.2m	8.8M

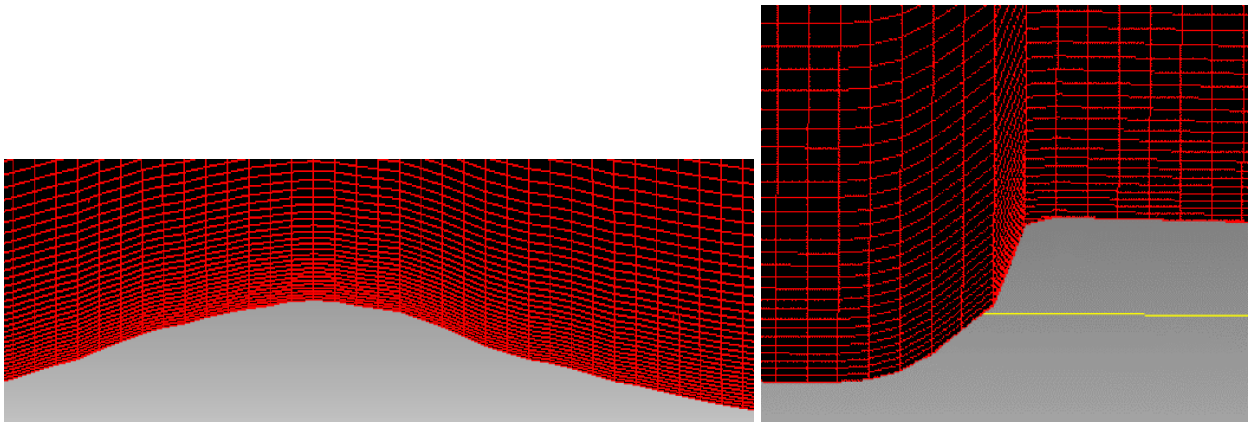

Figure 3-5. Askervein hill mesh (left) and Bolund hill mesh (right) over the hills depicted in gray. The wind direction flows from left to right and Bolund hill has a steep rise on the up-wind face before hitting the top of the hill.

The one-equation LES turbulent flow model was used in each terrain simulation. Instantaneous snapshots are shown for both hills at Fig. 3-6, at selected planes in the domain. While moderate

curvature of the flow structure is observed in Askervein hill case, the Bolund hill case shows strong flow interaction between the ground and the incoming turbulence.

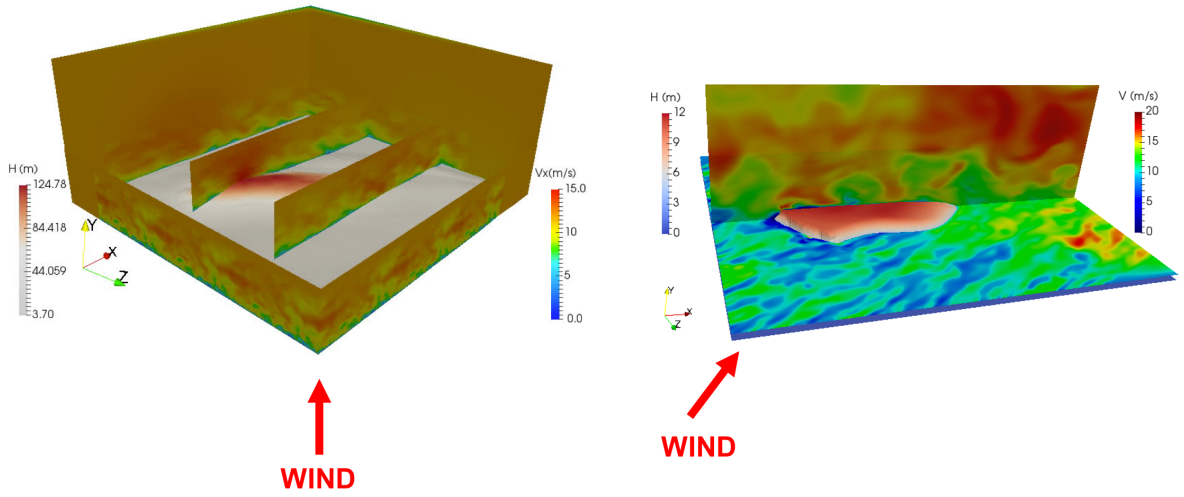

Figure 3-6. Velocity contours at several planes for Askervein (left) and Bolund (right) hills.

Figure 3-7 compares time-averaged velocity profiles from several mesh resolutions as well as experimental data along four marked lines for the Askervein hill case. Speed up is calculated as

$$\frac{V}{V_{inlet}} - 1 \tag{3.1}$$

where V is the time-averaged velocity. The speed up indicates how much acceleration or deceleration has occurred compared to the inlet velocity (V_{inlet}) on each streamline.

The result agrees with the experiment up to the point where the flow reaches the hill, where slightly better results were observed with refined meshes. An extrapolated result can be obtained using results from three different resolutions to approximate results from an extremely fine mesh resolution [6]. Such profile is marked as 'extrapolated' which occasionally diverges. Grid convergence index, which quantifies convergence rate between the resolutions [18], is plotted as an error bar on the fine mesh result. Note that these concepts are developed for RANS-based models and LES does not guarantee convergence of the solution with increasing mesh resolution.

The Bolund hill result is compared to the wind-tunnel and the field data in Figure 3-8 [3]. The LES results closely match the wind tunnel profiles but not the field data which is difficult to model since the exact wind condition is difficult to replicate in the simulations or wind-tunnel. We note that the wind direction and speed changes over the span of the averaging time frame and only the averaged speed and direction were used for the wind-tunnel experiment and the simulations. A systematic approach for control of the inflow speed and direction over time may be needed for better results.

Figure 3-9 includes results from Golaz [9] for the Askervein hill case and a blind study with several model predictions for the Bolund hill case [4]. While the mesh resolutions and numerical

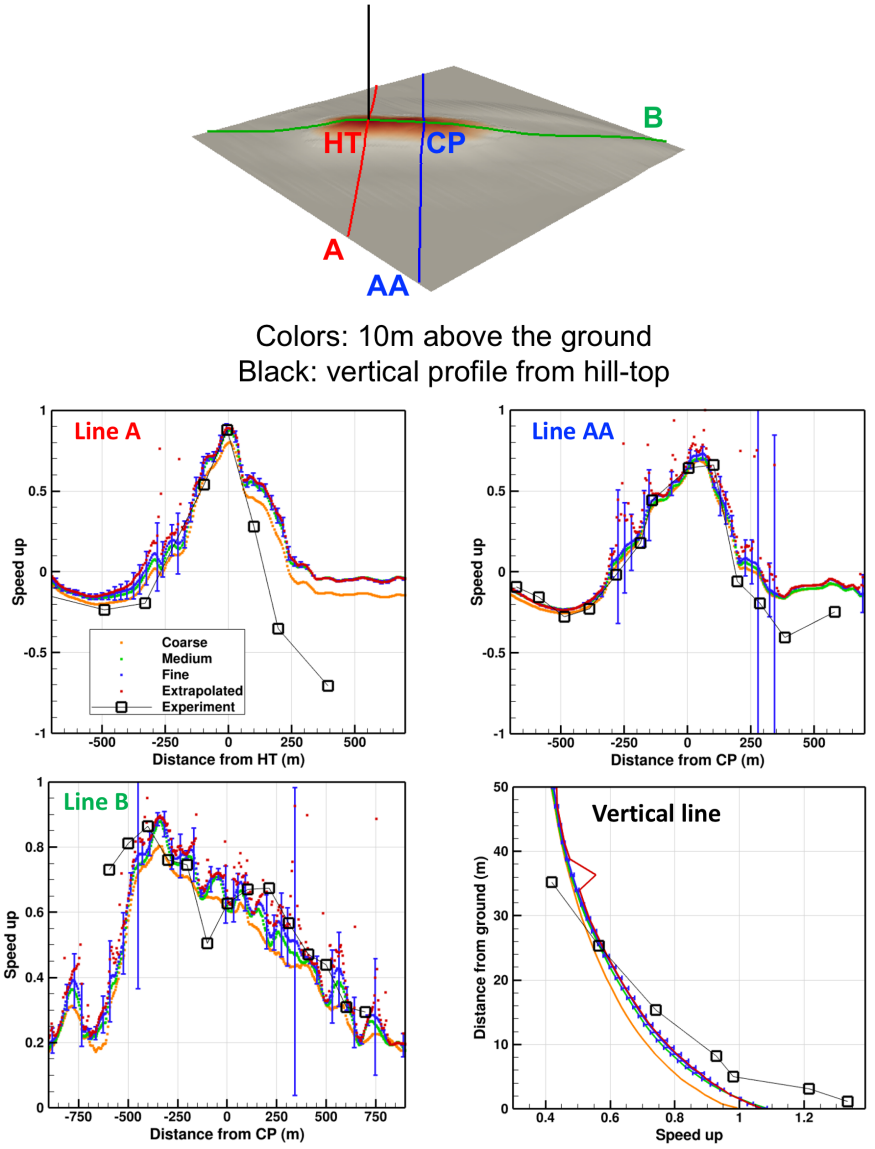

Figure 3-7. Speedup line plots at several comparison lines around the Askervein hill.

approaches are all different, predictions from Fuego lay mostly within the spread of other predictions with a tendency to over-predict the average velocity downwind from each of the hills.

The Bolund and Askervein hill scenarios are tests that have been documented as community validation conditions. These are primarily focused on the ability to predict terrain dynamics in flow codes in support of wind power applications. They have relevance to general prediction of flow for atmospheric conditions over terrain outside of the wind power application. The scenarios have historically yielded a range of simulation accuracy. A primary issue with these is that the models require an inflow boundary condition, which cannot be compared to the test conditions because the computational domain is vastly larger than the source flow data. Despite this uncertainty, models have historically compared moderately well to the data. The SIERRA/Fuego

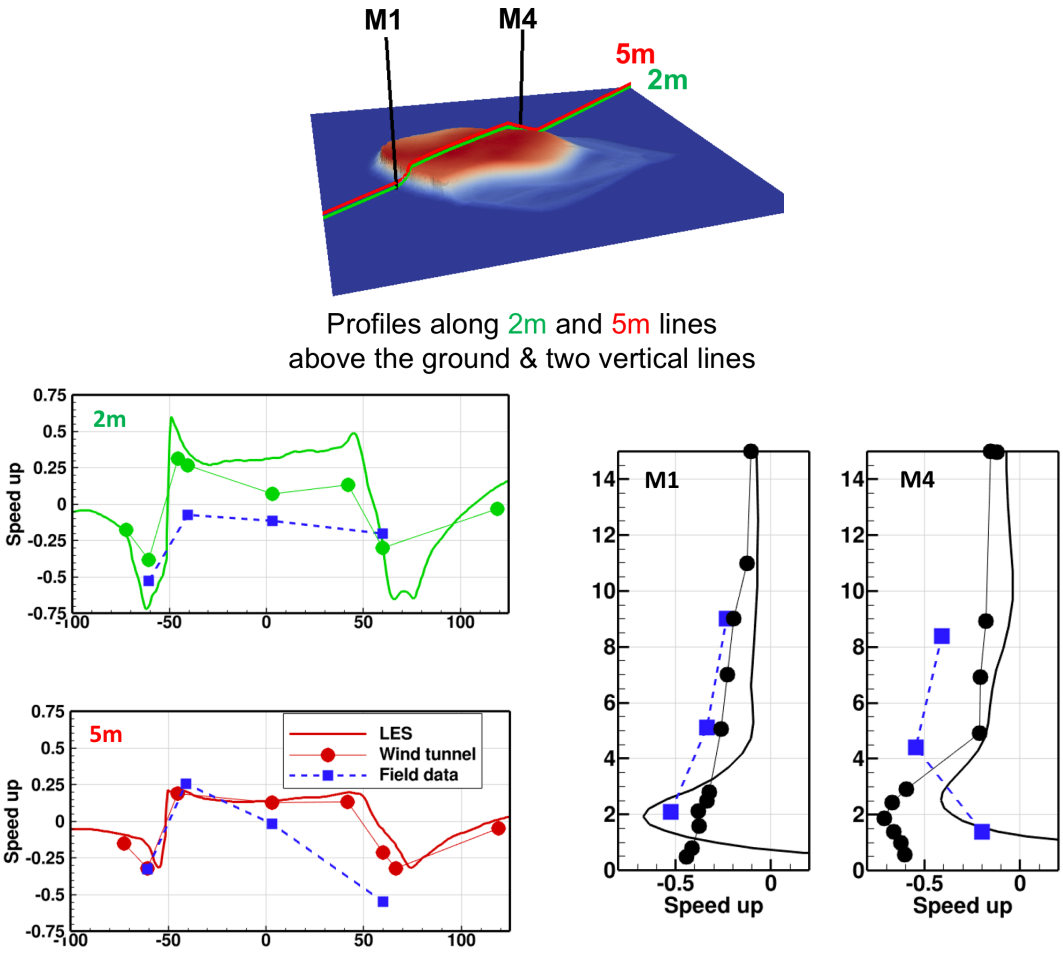

Figure 3-8. Speedup line plots for velocity around the Bolund hill where solid lines = LES results, filled circles = wind tunnel data, and filled squares = field data. The top figure shows the location of each line on the hill.

predictions also compared well and generally display the same trends as the experimental data and with the model predictions from other simulation tools. The inference we draw from this work is that the inflow methodology and the predictive capability of SIERRA/Fuego is approximately similar to that found in other codes. The methods are capable of making a reasonable reproduction of the large-scale terrain based wind behavior.

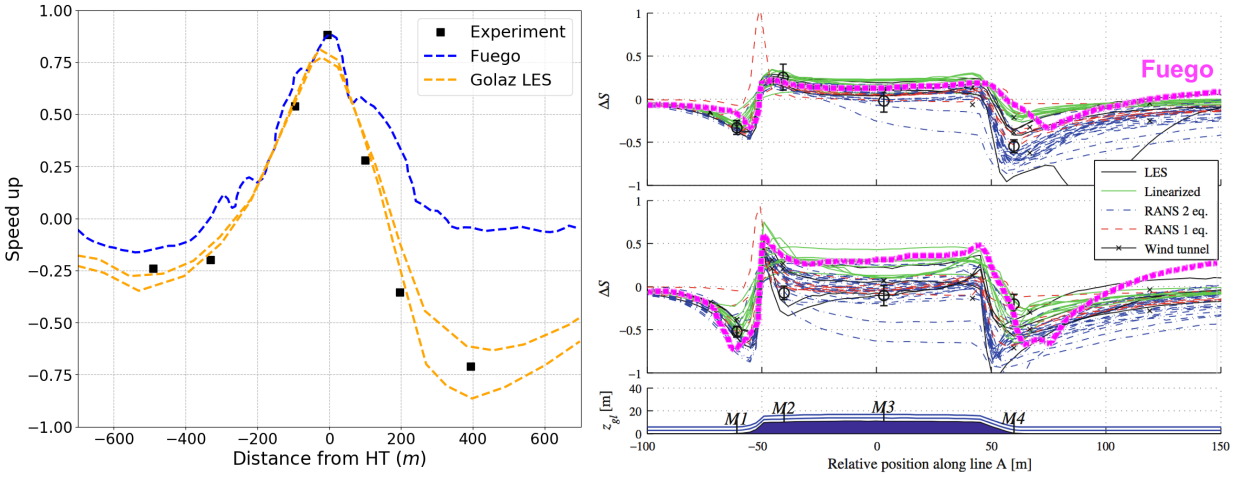

Figure 3-9. LES results from Fuego compared to experiments and simulation results from literature. On the left is the 'line A' of the Askervein hill compared to LES from Golaz [9]. The right plots are 5m (upper right) and 2m (lower right) lines above the ground on the Bolund hill case compared to simulations [4].

3.2. Open Jet Pipe Inflow

Unlike the larger-scale terrain example, modeling an application with open jet boundary conditions requires the modeler closely matching the Reynolds number to achieve acceptable predictions. While the theoretical transition from laminar to turbulence is approximately 2100, the minimum Reynolds number for retaining turbulence rises to approximately 4000 or higher when using CFD solvers due to numerical diffusion.

An open jet is simulated to demonstrate how an inflow file generated from an auxiliary simulation is practically used and to evaluate LES model performance. An air jet experiment by Amielh et al. [1, 7] is used as a basis for comparison. A cylindrical mesh is used with a total of 0.3M elements, and 16 elements span the jet inlet highlighted in Figure 3-10. For this flow, the Reynolds number is 21,000 and downstream measurements were made at several locations. The bulk velocity of the jet is 12 m/s and the coflow velocity is uniform at 0.9 m/s. An inflow file that was generated for a pipe using a Reynolds number of 18,000 was rescaled for this problem.

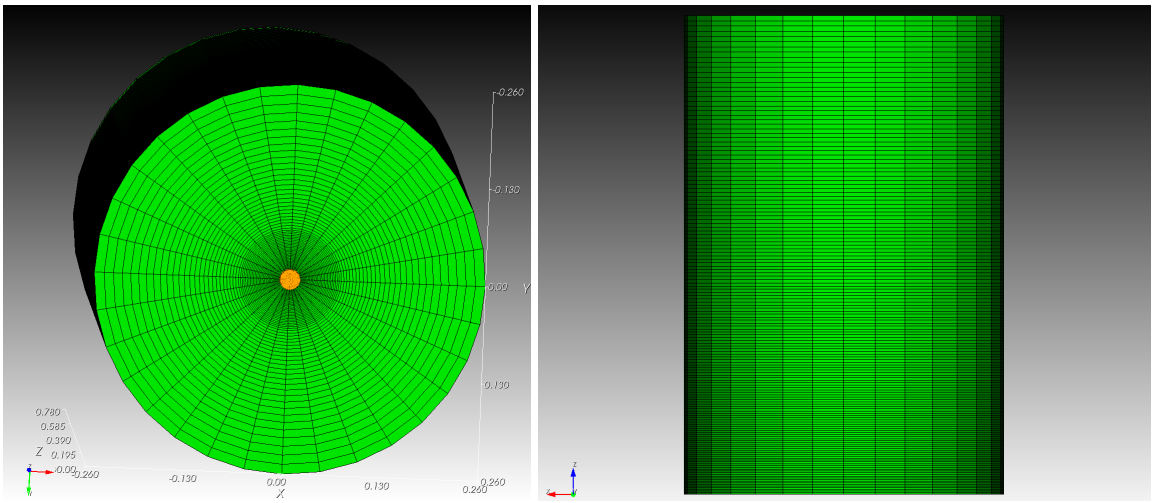

Figure 3-10. Bottom view of jet mesh with inflow surface highlighted (left), and side view of jet mesh (right).

The normalized axial velocity profiles from several LES models as well as an under-resolved DNS are compared to experimental data in Figure 3-11. The flow is averaged over a large number of flow periods following verification that a statistically stationary state was reached by computing statistics over time windows of different sizes. Under-resolved DNS suffers from the lack of viscosity, resulting in an oscillatory profile. The dynamic Smagorinsky and dynamic one-equation models follow the experimental profile well, while both models show delayed jet breakup. Dynamic models offer smaller turbulent viscosity than non-dynamic models, which induces a faster jet breakup and a better prediction in this particular configuration. However, in many simulations, dynamic models may lead to numerical instability. Both non-dynamic LES models over-predict the length at which jet breakup begins to occur.

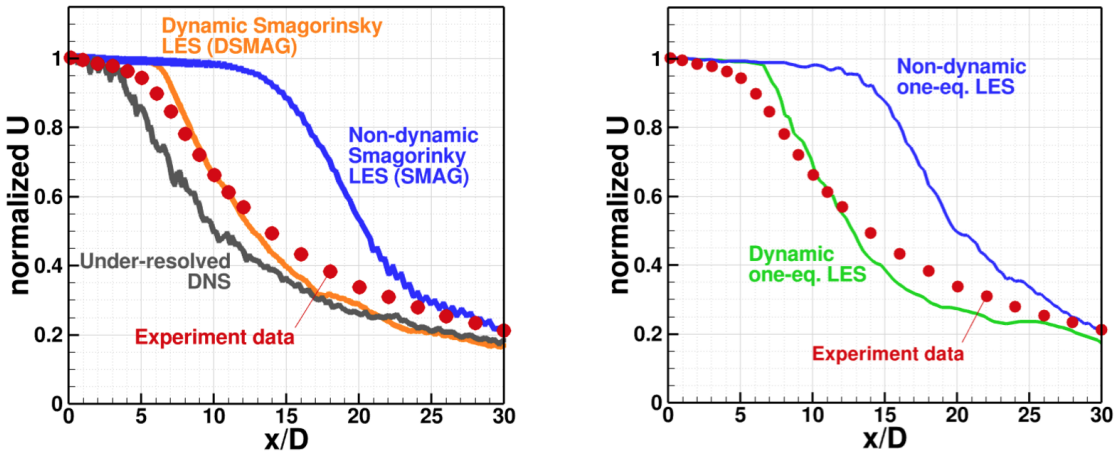

Figure 3-11. Normalized axial velocity profiles of different models in Fuego compared to the experimental data [1, 7].

4. CONCLUSION

The capability of Fuego to model wall-bounded flows has been demonstrated using simple channel and pipe configurations and the effects of wall model formulation for LES models have been studied. The goal of these investigations was to provide a method for creating auxiliary simulations using simple geometries and applying their resulting velocity predictions to inflow boundaries in more complex scenarios. It was found that by using a layered mesh for DNS at moderate Reynolds numbers Fuego performs well and the velocity profile closely matches the log-law profile. Using an equilibrium wall model LES also performs well, matching the log-law profile even for very large Reynolds numbers, but the viscous sublayer does not match using the wall model approaches.

Channel and pipe results were successfully used as inflow boundary conditions for larger problems. On terrain configurations, the bottom half of the channel flow was used as a fully developed boundary layer. The dimensions were chosen to match mean profile of the atmospheric boundary layer. Due to the large domain size, the grid size is on the order of meters, which pushes the limit for the existing LES regime. The results match the experiments well and results from Fuego lie within the range other modelers' predictions compiled in the comparative study. Pipe flow was used for an open jet where a fully developed inflow was replaced by the pipe DNS or LES. Using the inflow file, open jet predictions match when dynamic LES models are used. This particular configuration is sensitive to the jet breakup which depends on lower turbulent viscosity approaches such as dynamic models.

REFERENCES

[1] M. Amielh, T. Djeridane, F. Anselmet, and L. Fulachier. Velocity near-field of variable density turbulent jets. *International Journal of Heat and Mass Transfer*, 39(10):2149–2164, 1996.

[2] Andreas Bechmann. The bolund experiment. http://www.bolund.vindenergi.dtu.dk/the_bol

und_experiment. Accessed: 2019-07-18.

[3] J. Berg, J. Mann, A. Bechmann, M. S. Courtney, and H. E. Jorgensen. The bolund experiment, part I: Flow over a steep, three-dimensional hill. *Boundary-Layer Meteorology*, 141:219–243, 2011.

[4] J. Berg, J. Mann, A. Bechmann, M. S. Courtney, and H. E. Jorgensen. The bolund experiment, part II: Blind comparison of microscale flow models. *Boundary-Layer Meteorology*, 141:245–271, 2011.

[5] Alexander Brown and Erik Benavidez. Dispersion validation for flow involving a large structure. Number 2018-9380, 2018.

[6] Ishmail B Celik, Urmila Ghia, Patrick J Roache, and Christopher J Freitas. Procedure for estimation and reporting of uncertainty due to discretization in cfd applications. *Journal of fluids Engineering-Transactions of the ASME*, 130(7), 2008.

[7] T. Djeridane, M. Amielh, F. Anselmet, and L. Fulachier. Velocity turbulence properties in the near-field region of axisymmetric variable density jets. *Physics of Fluids*, 8(6):1614–1630, 1996.

[8] T. D. Economon, F. Palacios, S. R. Copeland, T. W. Lukaczyk, and J. J. Alonso. SU2: An open-source suite for multiphysics simulation and design. *AIAA Journal*, 54(3):828–846, 2016.

[9] Jean-Christophe Golaz, James D Doyle, and Shouping Wang. One-way nested large-eddy simulation over the askervein hill. *Journal of Advances in Modeling Earth Systems*, 1(3), 2009.

[10] F. Jaegle, O. Cabrit, S. Mendez, and T. Poinsot. Implementation methods of wall functions in cell-vertex numerical solvers. *Flow, Turbulence and Combustion*, 85(2):245–272, 2010.

[11] Nicolas Jarrin, Sofiane Benhamadouche, Dominique Laurence, and Robert Prosser. A synthetic-eddy-method for generating inflow conditions for large-eddy simulations. *International Journal of Heat and Fluid Flow*, 27(4):585–593, 2006.

[12] A. Keating and U. Piomelli. A dynamic stochastic forcing method as a wall-layer model for large-eddy simulation. *Journal of Turbulence*, 7(12):1–24, 2006.

[13] Markus Klein, Amsini Sadiki, and Johannes Janicka. A digital filter based generation of inflow data for spatially developing direct numerical or large eddy simulations. *Journal of computational Physics*, 186(2):652–665, 2003.

[14] AG Kravchenko, P Moin, and R Moser. Zonal embedded grids for numerical simulations of wall-bounded turbulent flows. *Journal of Computational Physics*, 127(2):412–423, 1996.

[15] M Lateb, Robert N Meroney, M Yataghene, H Fellouah, F Saleh, and MC Boufadel. On the use of numerical modelling for near-field pollutant dispersion in urban environments- a review. *Environmental Pollution*, 208:271–283, 2016.

[16] S Lee, S Lele, and P Moin. Simulation of spatially evolving compressible turbulence and the application of taylors hypothesis. *Phys. Fluids A*, 4(1521-1530):14, 1992.

[17] R. D. Moser, J. Kim, and N. N. Mansour. Direct numerical simulation of turbulent channel flow up to Re_τ=590. *Physics of Fluids*, 11(4):943–945, 1999.

[18] W. L. Oberkampf and C. J. Roy. *Verification and validation in scientific computing*. Cambridge University Press, 2010.

[19] Ugo Piomelli and Elias Balaras. Wall-layer models for large-eddy simulations. *Annual review of fluid mechanics*, 34(1):349–374, 2002.

[20] Sandia National Laboratories. *SIERRA Low Mach Module: Fuego User Manual – Version 4.42, SAND2016-10164*, 2016.

[21] P. A. Taylor and H. W. Teunissen. The askervein hill project: overview and background data. *Boundary-Layer Meteorology*, 39:15–39, 1987.

[22] Peter A Taylor. Askervein hill project reports. http://www.yorku.ca/pat/research/Askervein/. Accessed: 2019-07-18.

[23] Yoshihide Tominaga and Ted Stathopoulos. Cfd modeling of pollution dispersion in a street canyon: Comparison between les and rans. *Journal of Wind Engineering and Industrial Aerodynamics*, 99(4):340–348, 2011.

DISTRIBUTION

Email—Internal [redacted]

Name	Org.	Sandia Email Address
Carlos Lopez	1532	carlope@sandia.gov
Alexander Brown	1532	albrown@sandia.gov
Jeffrey Engerer	1532	jengere@sandia.gov
Walt Gill	1532	wgill@sandia.gov
John Hewson	1532	jchewso@sandia.gov
Andrew Kurzawski	1532	akurzaw@sandia.gov
Anay Luketa	1532	aluketa@sandia.gov
Randy Shurtz	1532	rshurtz@sandia.gov
Jill Suo-Anttila	1532	jmsuoan@sandia.gov
Caroline Winters	1532	cwinte@sandia.gov
Ethan Zepper	1532	etzeppe@sandia.gov
Technical Library	1911	sanddocs@sandia.gov

Sandia National Laboratories

Sandia National Laboratories is a multimission laboratory managed and operated by National Technology & Engineering Solutions of Sandia LLC, a wholly owned subsidiary of Honeywell International Inc., for the U.S. Department of Energy's National Nuclear Security Administration under contract DE-NA0003525.